www.tubiad.org
ISSN:2148-3736
El-Cezerî Fen ve Mühendislik Dergisi
Cilt: 2, No:1, 2015 (68-77)

El-Cezerî Journal of Science and Engineering
Vol: 2, No: 1, 2015 (68-77)

ECJSE

Makale / Research Paper

Continuous Wave Diffuse Optical Tomography System with High Resolution Current to Voltage Analog Digital Converter

Hüseyin Özgür Kazancı, Murat Canpolat*

Biomedical Optic Research Unit, Department of Biophysics, Medical School, Akdeniz University, Antalya 07058, Turkey
canpolat@akdeniz.edu.tr

Received/Geliş: 07.08.2014 **Revised/Düzeltme:** - **Accepted/Kabul:** 19.08.2014

Abstract: Diffuse Optical Tomography (DOT) systems are becoming popular for research purposes. In DOT systems there are some obstacles that have to be solved such as, low noise to signal ratio, short acqusition time and the system calibration. We have developed a DOT system with less enery consumption and less component. In this work, DDC232 integrated curcit (IC) chip has been used. Continuous Wave (CW) DOT system for back reflection geometry has been designed. The system has one back-reflection probe which has 49 source fibers and 49 detector fibers. The laser light sent into the tissue-like phantom from the each source fiber via switching by optical switch. The reflected light have been picked up by the detector fibers and directed to the photodetectors then the currents have been converted to 20 bit resolution digital voltages. Digital data have been acquired by one microcontroller then microcontroller has sent collected data to the PC via the NI Labview PC interface program.

Keywords: Continuous Wave (CW), Diffuse Optical Tomography (DOT) System, Analog to Digital Converter (ADC), Optical Switch.

1. Introduction

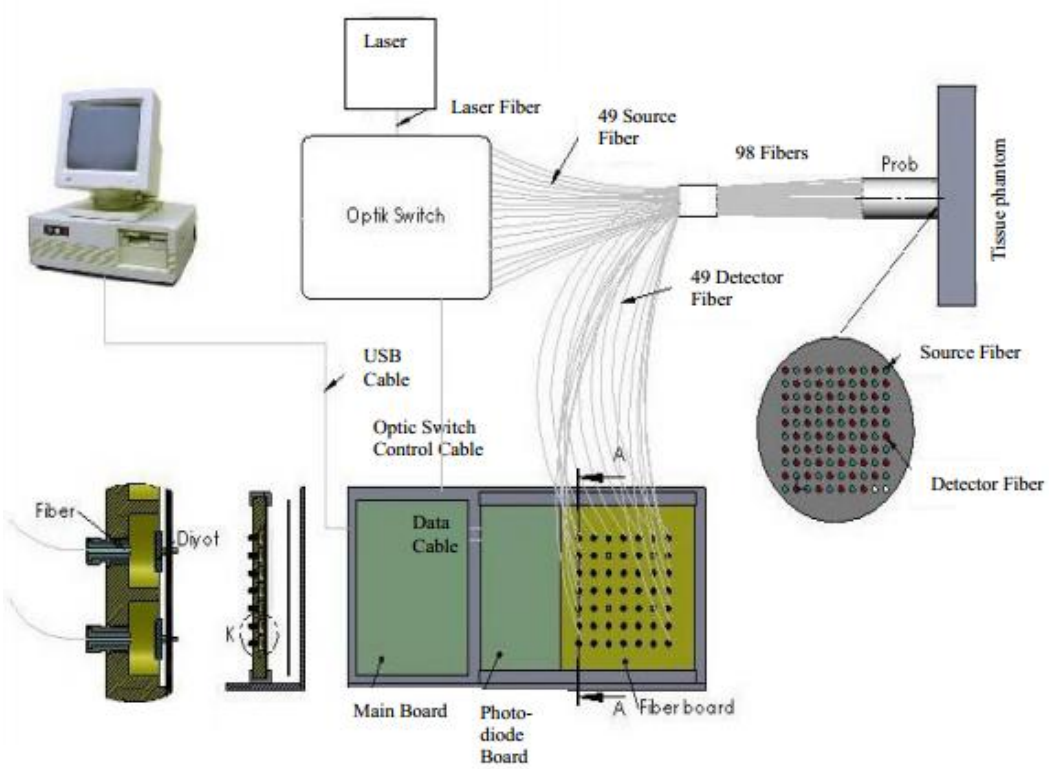
Continuous Wave (CW) diffuse optical tomography (DOT) systems are not harmful to the body by using non-ionising, low power laser. They are cheaper and easy transportable. They can be used in-vivo measurements. Scanning and image reconstruction time is short. But due to the decreased intensity of light as a result of absorption and scattering of tissue imaging depth is limited. Last 2 decades, DOT systems have been used such as breast and brain imaging [1-5].

Tissue includes hemoglobin, fat and water. Hemoglobin primarily absorbs photons at NIR wavelengths (700-900 nm), so the distribution of hemoglobin could be seen in the reconstructed images. Different mathematical algorithmic techniques are being used for DOT systems. These techniques include two models. One of them is forward model where, photon path distributions are calculated when the photons travel from the source position to the detector position in tissue. This is forward problem. The perturbation data which is back reflected from tissue have been used in linear reconstruction methods and Algebraic Reconstruction Technique (ART) is used to solve the equation system. Inverse problem uses optimization algorithm and regularization techniques to minimize the difference between the models predicted data and measured data [6].

How to cite this article
Kazancı, HO, Canpolat M, "*Depth normalization algorithm for continuous wave reflectance diffuse optical tomography system*" El-Cezerî Journal of Science and Engineering, 2015, 2.(1); 68-77.

2. System

The CW DOT system which has been designed is shown in Figure 1. The CW DOT system runs in a back-reflected geometry. 800 nm wavelength laser is used in the system. System includes, one laser source, 1x50 optical switch, one probe which has 49 source and 49 detector optical fibers, one computer, system electronics which has main electronic board and photodiode electronic board. The laser is switched from one source fiber to other by optical light switcher sequentially. By the optical switching system the light is switched to output by intended time of periods. When the laser in one source position, all acquised data from the all detectors have been transferred into the computer and then when the laser switched on the next source position the same process repeated. Optical probe is 10x10 optical fiber matrix. All the source and the detector fibers of the probe placed on a 10x10 matix. Top view of design is shown in Figure 2. The diameter of optical source and detector fibers is 1 mm. Distance between source and detector fibers is 3 mm. On probe there is totally 49 source and 49 detector optical fibers which collect scattered laser photons from tissue. Last source and detector fiber holes are empty as shown in Figure 1. The system has two electronic boards. One of them is photodiode board which collects scattered and absorbed laser photons back reflected from tissue. Detector fibers convey laser photons which is back reflected from tissue. Electric current is produced by photodiodes which collect back reflected laser photons. The photodiode board has 49 photodiode detectors and also two Texas Instruments & Burr-Brown DDC232 Current-to-Voltage Integrator & Analog to Digital Converter (ADC). These two chip converts 49 photodiode currents to the 49 analog voltages and then converts these 49 analog voltages to all bunch of digital data. These digital data are collected by main electronic board. The data acquisition from photodiodes, the control of electronic blocks, optic switching for source fibers, communication with computer are all done by main electronic board which has one microcontroller on it. On computer side Labview program is running. Labview program is communicating with microcontroller (PIC18f2550, Microchip) which is chief of main electronic board. Labview program is ordering its tasks to microcontroller. Main board is communicating via the USB cable. Communication is done by serial bus protocol.



Fifure 1. DOT system overview

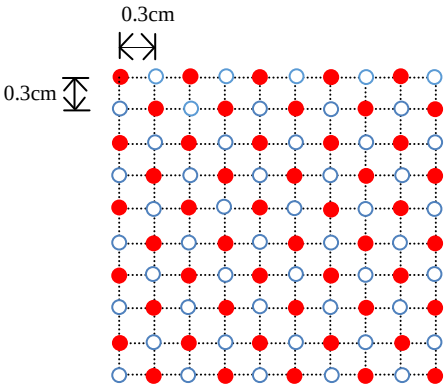


Figure 2. Top view of fiber probe.

Top view of source-detector matrix design is given in Figure 2. Source fibers are red and detector fibers are blue. There is 3 mm between two consequent fibers. It is aimed to scan tissue of the semi-infinite volume, and wanted to get more information from tissue or tissue-like phantom. Through this design totally 22 neighbourhood relationships have been used. There are 49x49=2401 measurement data. System has photodiode electronic board and main electronic board. On photodiode electronic board there are 49 photodiodes and two DDC232 ADC chips. On main electronic board there is one microcontroller, connectors and other electronic components. The block diagram of DOT system detectors connection is shown in Figure 3. Photodiodes are light sensitive semiconductor electronic elements. Photodiodes are generating current depend on laser light back reflected from the tissue. In the system, OSD35-LR-D photodiodes (OSI Optoelectronics) have been used. The currents which are generated by photodiodes on detector board are integrated to analog voltages by DDC232 ADC chips and then converted to digital data. They use delta-sigma modulators for ADC processing.

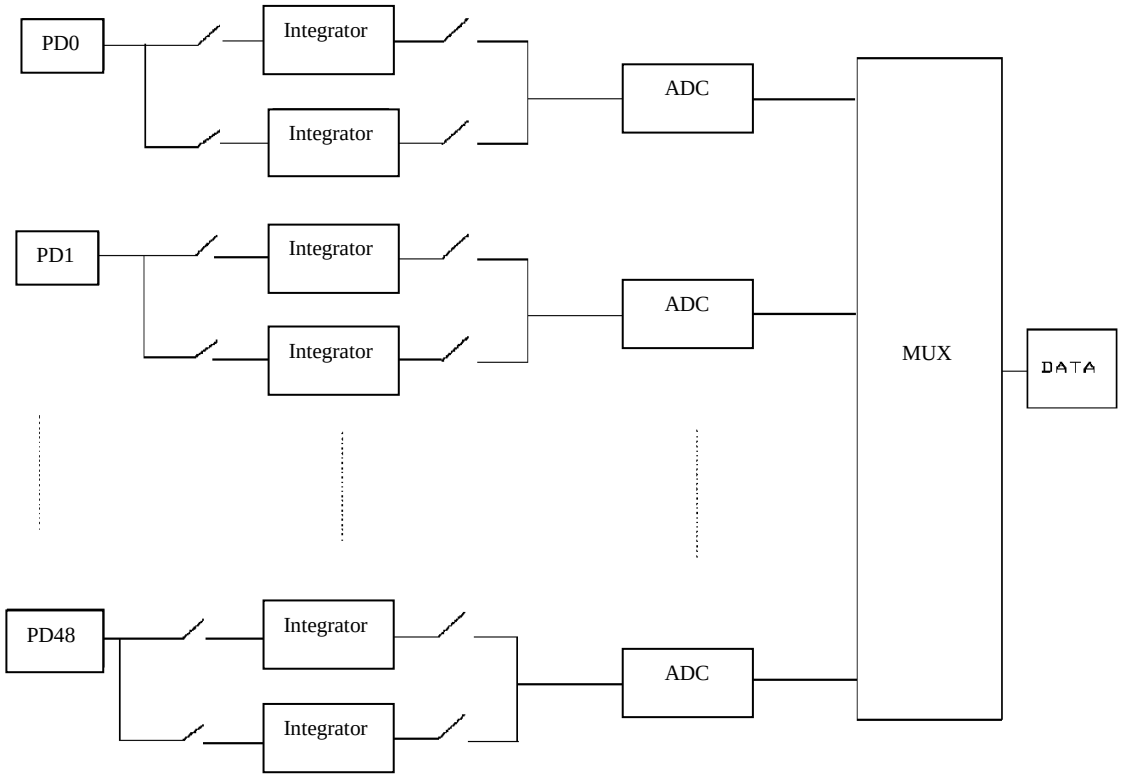


Figure 3. Block diagram of DOT system detectors connection.

Between each photodiode and DDC232 integrated circuit (IC) ADC converter, there are two integrators and four switches. In the input side, these two switches achieve integrating process continuously. When one of the switch is on, the integrator is connected to this switch integrates photodiode current to analog voltage; the other circuit is connecting to ADC and connecting the analog voltage to delta-sigma ADC modulator. For each of the 32 inputs, the DDC232 provides a dual-switched integrator front-end. This configuration allows for continuous current integration: while one integrator is being digitized by the onboard A/D converter, the other is integrating the input current. Adjustable integration times range from 166 ms to 1s, allowing currents from fAs to mAs to be continuously measured with outstanding precision [7]. In DDC232 IC, integrating, ADC converting, multiplexing and integration time control can be done. IC package is BGA (Ball Grid Array). This makes it extremely small. DDC232 IC is key factor for this system. After implementation of the system, it has been calibrated. Optic-switch for each of the source fiber position has been moved to gather measurement data for each source fiber position.

3. Phantom Experiment

Calibration system has been tested by phantom experiments. In the experiment, 4000 ml intralipid tank with μ_s'=10 cm^{-1} absorption coefficient has been used as a breast tissue phantom and spherical indocyanine-green (ICG) inclusion with μ_a=0.73 cm^{-1} absorption coefficient has been put into tank. The diameter of spherical inclusion is almost 6-8 mm. Symbolic representation of inclusion is shown in Figure 4.

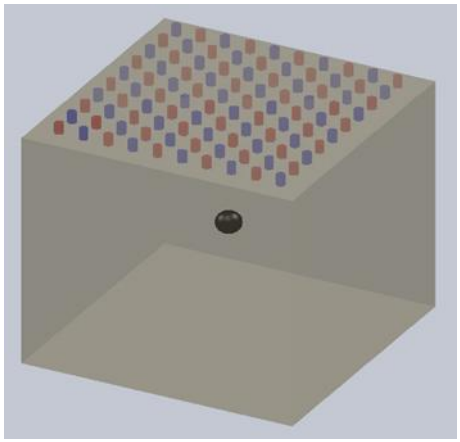


Figure 4. Experimental setup.

4. Reconstruction

After data acquisition, the linear equation system in y = Ax form has been solved in the reconstruction process. In this equation system y vector is the perturbation data, A matrix symbolizes weight matrix which is correlating between voxels and source-detector couplings; x vector is the average absorption coefficients of the voxel in the region of interest. Number of elements of y vector is the source-detector couplings; Number of elements of x vector also equals number of voxels in semi-infinite space. Number of rows of weight vector equals source-detector couplings. Number of columns of weight vector equals voxels number. Thus, deeper voxels have small weight function coefficients, their effects are ignored. When the inverse solution is applied image of the inclusion shifts to the tissue surface. In order to prevent this negative effect, weak voxels power has to be gained. To do this DCA algorithm has been used [8] and weight matrix has been updated by this method. Linearized equation system is:

$$y=Ax \quad (1)$$

linearized equation system form, inverse problem solution is:

$$x=(A^TA+\lambda I)^{-1}A^Ty \quad (2)$$

This is known as Tikhonov inverse problem solution and gives approximate solution. But as explained before if this inverse problem solution is used directly, unknown space absorption changes or concentrations does not give exact solution. Instead of A weight matrix replaced by $A^{\#}$ matrix. The reconstructed images approach to real one. The replaced weight matrix $A^{\#}$ is as follows: Voxels are grouped into same depth layers. Weight matrix A is also grouped into same layer classifications. Each of the sub matrixes are divided into same depth layer group, singular values are measured by Singular Value Decomposition (SVD) method. For all singular values in submatrixes, maximum singular values are calculated. These maximum singular values are switched and put into weight matrix. Switching is as follows: To ensure DCA method; singular value maximum for deeper layer is switched by singular value maximum for upper layer; against it singular value maximum for upper layer is switched by singular value maximum for deeper layer. There are totally 10 layers, so switching is as follows: 1-10:10-1, 2-9:9-2, 3-8:8-3, 4-7:7-4, 5-6:6-5. Then diagonal matrix has been constructed which has maximum singular values of each submatrix. This new matrix has same row and column elements of voxel numbers. Gamma parameter should be selected based on the depth of the lesion. The diagonal matrix has been constructed before is the T matrix. According to DCA method in [8] $A^{\#}$ is defined as Equation 3.

$$A^{\#} = A*\mathrm{diag}(T)^{\gamma} \quad (3)$$

Gamma parameter is crucial for this method. There is no direct method to estimate gamma parameter to define location of the inclusion correctly. In the literature [9-14], ultrasound and fMRI have been used to measure depth of the inclusions to guess gamma. Then they are using gamma parameter depending on inclusion depth. Lambda parameter has to be selected for Tikhonov solution space. Because lambda parameter selection is necessary for Tikhonov solution space. Researchers use different mathematical methods to select lambda parameter. In this study L-curve method has been used which is efficient for lambda parameter selection. For different solution norms there are different error norms. And which will be important is to select corner of L-curve. This corner be best lambda parameter for Tikhonov solution space. Flowchart to select best lambda parameter for algorithm has been shown in Figure 5. For the experiment the number of row elements 2401 is source-detector coupling measurements and number of column elements 1000 is same as number of voxel elements. In the flowchart, $A^{\#<i,*>}$ representation shows i_{th} column and all row elements of $A^{\#}$ updated weight matrix. For one column, all row elements of weight vector has been multiplied by all row elements of b vector independently. Then the all multiplications have been summed. The same process has been repeated for the all columns of updated weight matrix.

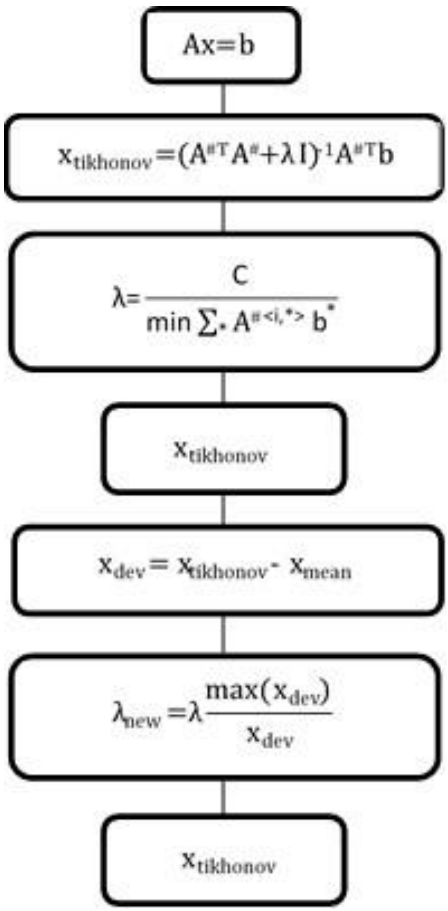


Figure 5. The block diagram of Tikhonov lambda parameter selection method.

4. Simulation Results

The weight matrix A which is defined for MC simulations has 2500x1000 element. Beacuse there is 1 more source and detector positions. Volume geometry has been divided into 10x10x10 equal voxels. Total voxel number is 1000. 50 sources and 50 detectors have been located in MC simulation. Source and detector fibers have been mounted on slab geometry surface. From the bird eye view 10x10 square could be seen. In simulations, source and detector fiber radius is 0.5 mm. Total square dimension is 1cmx1cm for MC simulation. Source and detector fibers are also tangential for MC simulations. In Figure 6. it could be seen that source and detector locations from top level and trimetric slab geometry. In MC simulations one inclusion has been put for each simulation. Inclusion radius is 0.5 mm. Inclusion is spherical. Inclusion has been put in 4 different coordinates. Goal is to determine gamma parameters correctly depending on the inclusion depth. X-y coordinate has been kept same and z depth coordinate has been changed. For x,y,z coordinate system, inclusions have been put in (0.5,0.5,0.1), (0.5,0.5,0.3), (0.5,0.5,0.5) and (0.5,0.5,0.7). For each source fiber position, photons have been propagated. Photon wavelength is 800 nm. For MC simulations there is totally 50x50=2500 source-detector coupling and whereat 2500 measurement data.

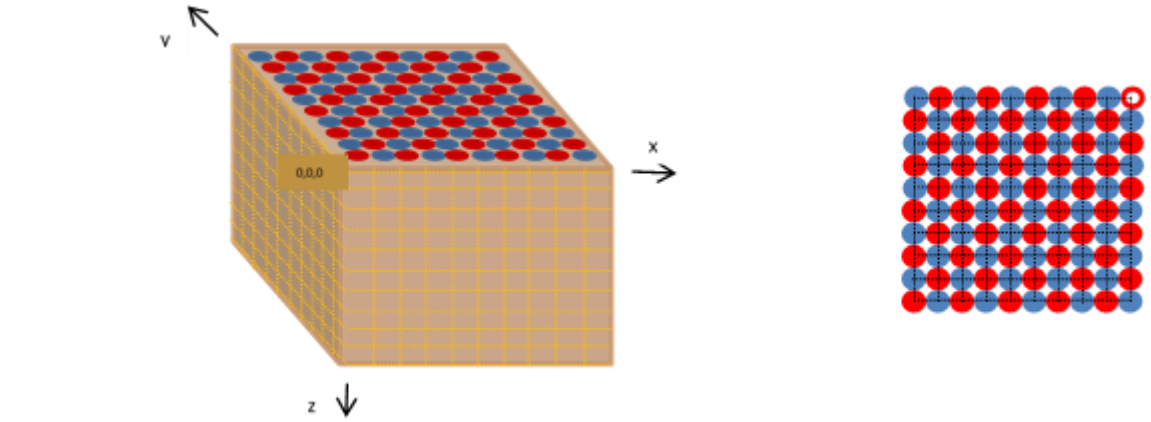


Figure 6. Source-detector locations for MC simulation (Red:Source, Blue:Detector).

While the images have been reconstructed all source-detector data have been used. A weight matrix is 2500x1000 overdetermined. In all measurement data there are 22 source-detector neighbourhood relationships. For MC simulations tissue-like background absorption coefficient is 0.0001 cm^{-1}. 5000000 photons have been sent for each source position. At 800 nm wavelength which photons have been sent inside the tissue-like intralipid phantom, absorption coefficient μ_a is almost 0. Reduced scattering coefficient μ_s' for tissue-like intralipid medium for MC simulation is selected 9.050 cm^{-1}. Absorption coefficient μ_a of spherical inclusion is 0.75 cm^{-1}. Volumetric reconstruction algorithm has been applied from x=0 to x=1 cm; from y=0 to y=1 cm; from z=0 to z=1 cm. Voxels are 0.1x0.1x0.1 cm^3. 10 equal DCA algorithm layers have been used. In Figure 7. depth layers could be seen. For each layer subweight matrixes have been constructed and maximum singular values have been calculated.

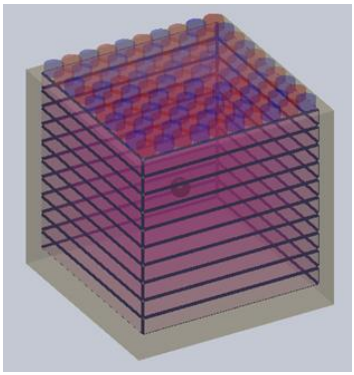
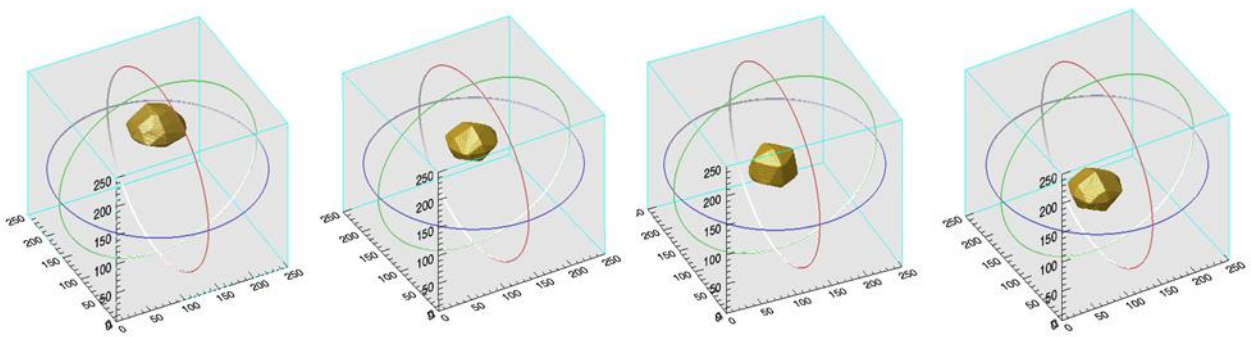


Figure 7. DCA algorithm depth layers.



0.1 cm in depth 0.3 cm in depth 0.5 cm in depth 0.7 cm in depth

Figure 8. Reconstructed inclusion images for different depth locations (simulation results).

4. In-Vitro Phantom Results

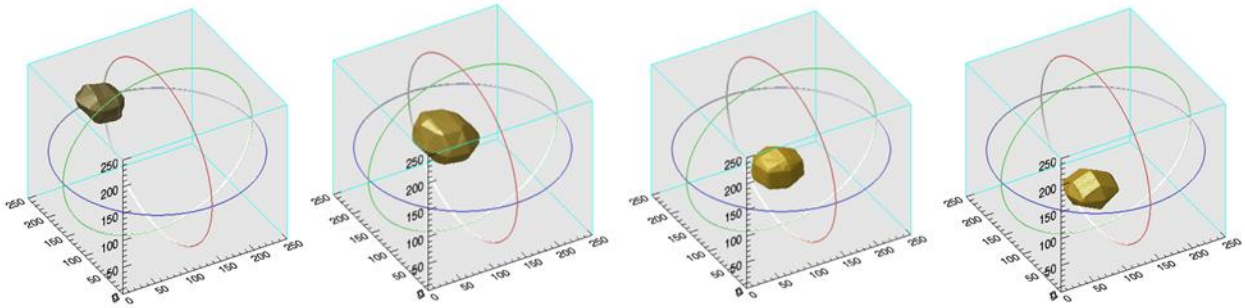


Figure 9. Reconstructed inclusion images for different depth locations (in-vitro phantom results).

In Figure 8. and Figure 9. reconstructed inclusion images for different depth locations have been shown. As could be seen from images that different inclusion depths can be realized. In this experiment the tank is pure intralipid and it is homogenuous.

5. Contrast To Noise Ratio (CNR) & Position Error (PE)

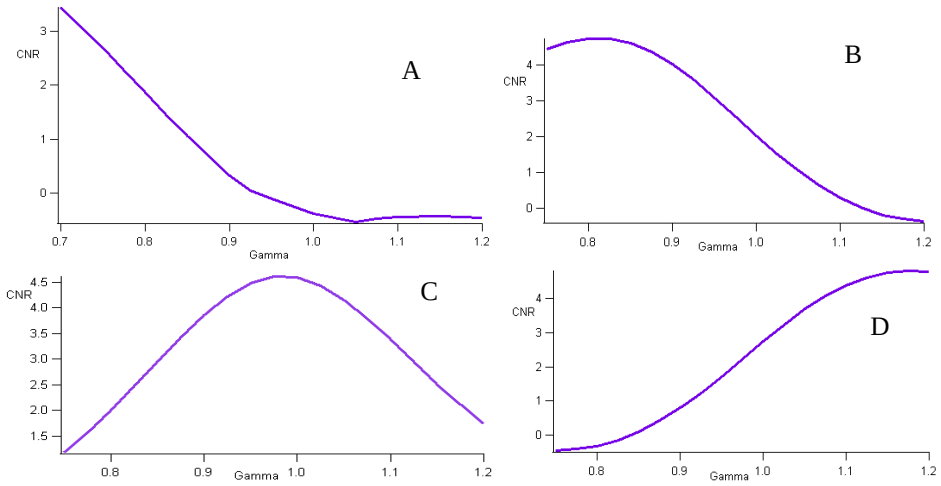
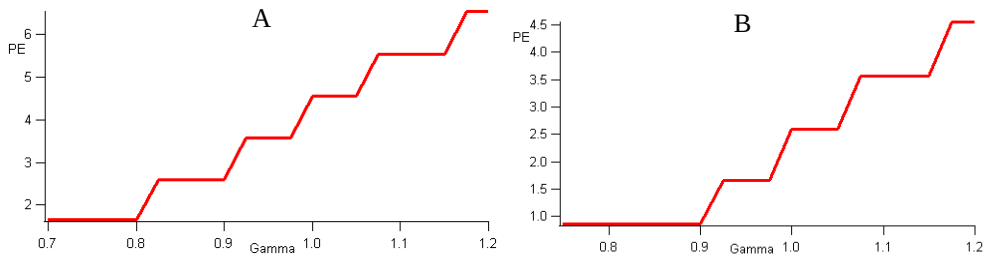


Figure 10. A. CNR vs Gamma for inclusion is in 0.1 cm depth, B. CNR vs Gamma for inclusion is in 0.3 cm depth, C. CNR vs Gamma for inclusion is in 0.5 cm depth, D. CNR vs Gamma for inclusion is in 0.7 cm depth.



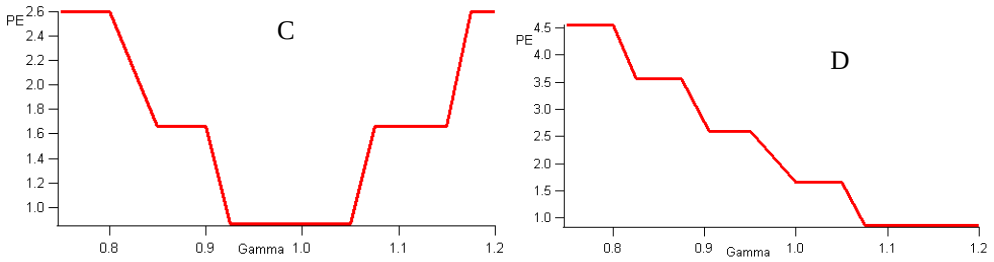


Figure 11. A. PE vs Gamma for 0.1 cm depth, B. PE vs Gamma for 0.3 cm depth, C. PE vs Gamma for 0.5 cm depth, D. PE vs Gamma for 0.7 cm depth.

6. Conclusion

Forward model has been created. Inverse problem solution algorithms have been applied. Perturbation vector has been constructed as mentioned earlier in literature [15]. Weight matrix coefficients have been created by forward model via MC simulations. Inverse problem solutions have been applied by Tikhonov regularization method. The most talented IC ADC has been used for the first time in DOT system. Thus data acquisition system has been minimized.

References

1. B. Yodh and B. Chance, "Spectroscopy and imaging with diffusing light," *Phys. Today* 48(3), 34–40 (1995).

2. H. Jiang, N. V. Iftimia, Y. Xu, J. A. Eggert, L. L. Fajardo, and K. L. Klove, "Near-infrared optical imaging of the breast with model-based reconstruction," *Acad. Radiol.* 9(2), 186–194 (2002).

3. Z. Yuan, Q. Zhang, E. S. Sobel, and H. Jiang, "Image-guided optical spectroscopy in diagnosis of osteoarthritis: A clinical study," *Biomed. Opt. Express* 1(1), 74–86 (2010).

4. Z. Yuan, "Combing independent component analysis and Granger causality to capture brain network dynamics with fNIRS measurements," *Biomed. Opt. Express* 4(11), 2629–2643 (2013).

5. R. C. Mesquita, M. A. Franceschini, and D. A. Boas, "Resting state functional connectivity of the whole head with near-infrared spectroscopy," *Biomed. Opt. Express* 1(1), 324–336 (2010).

6. S. Srinivasan, B. W. Pogue, S. Jiang, H. Dehghani, C. Kogel, S. Soho, J. J. Gibson, T. D. Tosteson, S. P. Poplack, and K. D. Paulsen, "Interpreting hemoglobin and water concentration, oxygen saturation, and scattering measured in vivo by near-infrared breast tomography," *Proc. Natl. Acad. Sci. U.S.A.* 100(21), 12349–12354 (2003).

7. Texas Instruments, "DDC232 32-Channel, Current-Input Analog-to-Digital Converter," www.ti.com, SBAS331D –AUGUST 2004–REVISED APRIL (2010)

8. H. Niu, F. Tian, Z.J. Lin, H. Liu, "Development of a compensation algorithm for accurate depth localization in diffuse optical tomography," *Optics Letters* 35(3), 429-431 (2010).

9. B. Tavakoli, Q. Zhu, "Improving Light quantification of large breast lesions imaged by diffuse optical tomography," *Optical Tomography and Spectroscopy of Tissue IX, Proceedings of the SPIE* 7896, 789618-789618-8 (2011).

10. B. Tavakoli, Q. Zhu, "Depth-correction algorithm that improves optical quantification of large breast lesions imaged by diffuse optical tomography," *J. Biomed Opt.* 16(5), 056002 (2011).

11. H. Niu, F. Tian, Z.J. Lin, H. Liu, S. Dhamne, "Comprehensive investigation of three-dimensional diffuse optical tomography with depth compensation algorithm," *J. Biomed Opt.* 15(4), 046005 (2010).

12. V.C. Kavuri, F. Tian, Z.J. Lin, H. Liu, "Sparsity enhanced spatial resolution and depth localization in diffuse optical tomography," *Biomedical Optics Express* 3(5), 943-957 (2012).

13. X. Song, B.W. Pogue, S. Jiang, M.M. Doyley, H. Dehghani, T.D. Tosteson, K.D. Paulsen, "Automated region detection based on the contrast-to-noise ratio in near-infrared tomography," *Applied Optics* 43(5), 1053-1062 (2003).

14. F. Tian, H. Niu, S. Khadha, Z.J. Lin, H. Liu, "Algorithmic depth compensation improves transverse resolution and quantification in functional diffuse optical tomography," *Optical Tomography and Spectroscopy of Tissue IX, Proceedings of the SPIE* 7896, 78960N (2011).

15. H.Ö. Kazancı, T. Mercan, M. Canpolat, "Design and evaluation of a reflectance diffuse optical tomography system," *Opt. Quant. Electron.*, 46/4 (2014).